Simulating transvertebral ultrasound propagation with a multi-layered ray acoustics model

Rui Xu, Meaghan A. O'Reilly

Sunnybrook Research Institute, Sunnybrook Health Sciences Centre, 2075 Bayview Avenue, Toronto, ON, M4N 3M5, Canada
Department of Medical Biophysics, Faculty of Medicine, University of Toronto, 101 College Street Suite 15-701, Toronto, ON M5G 1L7, Canada

E-mail: rxu@sri.utoronto.ca, moreilly@sri.utoronto.ca

Abstract.

The simulation accuracy of transvertebral ultrasound propagation using a multi-layered ray acoustics model based on CT-derived vertebral geometry was investigated through comparison with experimental measurements of pressure fields in *ex vivo* human vertebral foramen. A spherically focused transducer (5 cm diameter, f-number 1.2, 514 kHz) was geometrically focused to the centre of individual thoracic vertebral foramen, through the posterior bony elements. Transducer propagation paths through the laminae and the spinous processes were tested. Simulation transducer-vertebra configurations were registered to experiment transducer-vertebra configurations, and simulation accuracy of the simulation model was evaluated for predicting maximum transmitted pressure to the canal, voxel pressure in the canal, and focal distortion. Accuracy in predicting maximum transmitted pressure was calculated by vertebra, and it is shown that simulation predicts maximum pressure with a greater degree of accuracy than a vertebra-specific insertion loss. Simulation error in voxel pressure was evaluated using root-mean-square error and cross-correlation, and found to be similar to the water-only case. Simulation accuracy in predicting focal distortion was evaluated by comparing experiment and simulation maximum pressure location and weighted >50% focal volume location. Average simulation error across all measurements and simulations in maximum pressure location and weighted >50% focal volume location were 2.3 mm and 1.5 mm, respectively. These errors are small relative to the dimensions of the transducer focus (4.9 mm full width half maximum), the spinal cord (10 mm diameter), and vertebral canal diameter (15-20 mm diameter). These results suggest that ray acoustics can be applied to simulating transvertebral ultrasound propagation.

PACS numbers: 00.00, 20.00, 42.10

Keywords: Focused Ultrasound, Vertebral Column, Ray Acoustics

1. Introduction

Spinal cord disease can be devastating, as the spinal cord is central to motor control, sensation, and many autonomous reflexes. Spinal cord disease treatments are often ineffective, as spinal cord disease is often multifactorial and the blood spinal cord barrier (BSCB) severely limits drug delivery via the intraarterial/intravenous approach. The BSCB prevents the passage of the majority of molecules between the bloodstream and the spinal cord parenchyma, rendering most molecular treatments of the spinal cord ineffective [1]. Focused ultrasound can safely and transiently open the blood brain barrier (BBB) for the transport of drugs and genes across the BBB in animal models [2]. This technique has recently reached clinical trials and has the potential to drastically increase the possibilities for targeted drug therapies in the brain [3, 4, 5]. The extension of this technique to the human BSCB will similarly revolutionize targeted therapies to the spinal cord, and preliminary work in small animal model supports this hypothesis [6, 7, 8].

The spinal cord is encased by the spine, which consists of stacked, irregularly shaped vertebrae. Vertebrae have acoustic properties that differ drastically from soft tissues, posing a challenge for focusing ultrasound to the spinal cord for BSCB disruption [9, 10]. Safe and accurate delivery of focused ultrasound for BSCB disruption will require compensation for vertebra-induced phase and amplitude aberration. These compensations may be generated using phased arrays and appropriate phase and amplitude corrections. A range of methods for determining phase and amplitude exist, ranging from invasive hydrophone based methods [11, 12, 13, 14] to non-invasive methods based on pre-operative X-ray computed tomography (CT) or magnetic resonance imaging (MRI) scans [15, 16, 17, 18, 19]. Non-invasive methods are preferable for clinical translation, although the accuracy of non-invasive methods comes at computational cost [20].

Ray tracing, an analytical method where phase corrections are based on estimated time of flight derived from tissue properties along a ray directly between array element and target, can provide a first order approximation of phase correction at a minimal computational cost [21]. However, ray tracing fails to account for refraction, mode conversion, and reflection at interfaces, an important consideration for the highly irregular vertebral column, where ultrasound is likely to be incident at non-normal angles to the bone surface and the aforementioned effects must considered.

An approximate numerical model based on the Rayleigh-Sommerfeld integral accounts for the physics of acoustic waves incident on fluid-solid and solid-fluid interfaces, but remains much less computationally expensive than full-wave acoustic models [22, 23]. This model, often termed a 'multi-layered ray acoustics' model, was developed for modelling ultrasound propagation through the skull [24, 25, 16, 26, 27, 28, 29, 30, 31], and has since been extended to account for the heterogeneity of the acoustic properties of bone using CT intensity-derived densities, speeds of sound, and attenuation coefficients [32, 10, 33, 34]. The multi-layered ray acoustics model has

been successful for modelling transskull ultrasound propagation, however two major unknowns must be investigated to determine if the application of ray acoustics to the vertebral column is feasible. It is not known if the density-speed of sound and density-attenuation relationships for skull can be extended to vertebrae. It is also not known if the ray acoustics method is appropriate for the highly irregular vertebral geometry. The purpose of this study is to address these two unknowns through comparison of experimental measurements and ray acoustics simulations of ultrasound propagation through the posterior elements of *ex vivo* human vertebrae. The development of a validated acoustic model of the human spine will permit a broad range of studies to advance ultrasound interventions in the spinal column.

2. Materials and Methods

2.1. Experimental Setup

A dehydrated *ex vivo* adult human spine (Osta International, White Rock, BC, Canada) was reconstituted by submersion in a 10% buffered formalin for several months in order to restore the acoustic properties of the spine to close to its *in vivo* values [35, 36]. The age at death and sex of the spine donor were not provided, however, an analysis of vertebral body volume was performed and compared to [37], with average vertebral body volume 5.4% smaller than the average male specimen and 7.2% larger than the average female. There was no sign of vertebral pathology with the exception of minor ossification of the ligamentum flavum in T10. Over a period of several weeks, daily degassing of the vetebrae was performed in deionized water in vacuum jar to removed trapped air. All vertebrae were further degassed in a vacuum chamber (Nalgene vacuum chamber, Fisher Scientific; Gast, Benton Harbor, MI, USA) for several hours prior to being imaged with a CT scanner (Aquilone One, Toshiba). The vertebrae were oriented with the vertical axis aligned with the CT bore, as if they were *in vivo*. The vertebrae were then imaged with an isotropic resolution of approximately 0.5mm with the same CT settings as those used for skull to maximize the extensibility of skull acoustic parameters to vertebrae [38, 39, 40]. Even numbered thoracic vertebrae (T2, T4, T6, T8, T10, T12) were selected for the experiment, as the thoracic region presents a particular challenge for ultrasound delivery due to limited acoustic windows. Further, while in the lumbar and cervical spine the array aperture could potentially be increased by combining dorsal, medial and, in the cervical spine, possibly ventral approaches, the presence of the lungs and the rib cage limit thoracic interventions to a dorsal approach. These vertebrae were individually placed in the experimental setup shown in Figure 1.

A 5 cm diameter, 6 cm focal length spherically focused peizocomposite transducer with a fundamental frequency of 514 kHz was used to sonicate *ex vivo* human vertebrae. The transducer was assembled in-house (element purchased from DeL Piezo Specialties, LLC, West Palm Beach, FL, USA) and was electrically matched to 50Ω, 0° using an external matching circuit. The transducer was chosen for its focal characteristics (focal

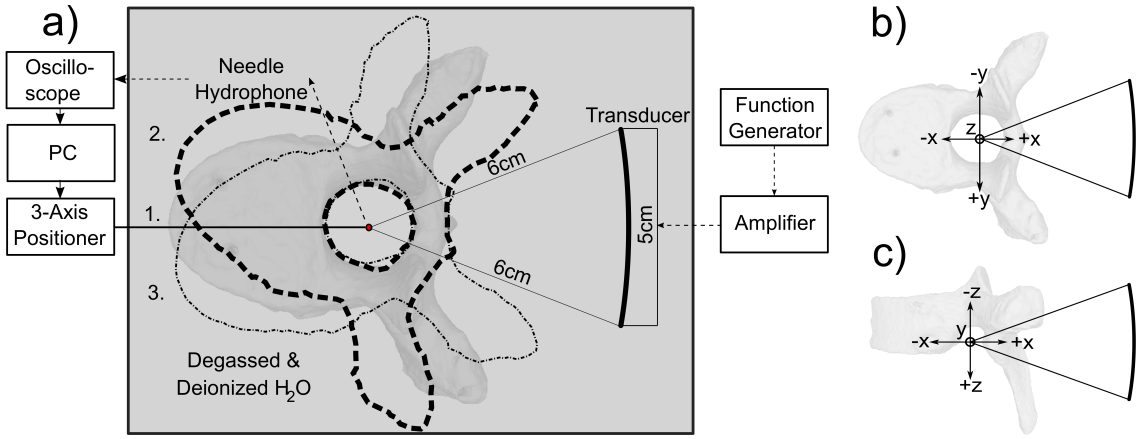

Figure 1. a) Experimental setup, with the tested transducer-vertebra configurations shown: 1. Transducer focused through posterior arch. 2. Transducer focused through right lamina. 3. Transducer focused through left lamina. The coordinate system is based on the geometric focus of the transducer. **b)** Superior view of the coordinate system. **c)** Lateral view of the coordinate system. Rubber-lined tank dimensions are $x = 90\,\text{cm}$, $y = 30\,\text{cm}$, $z = 30\,\text{cm}$. The transducer and vertebra are presented to scale relative to one another.

diameter 4.9 mm, approximately half the diameter of the spinal cord [41]), and the focal length, which is appropriate for focusing through the soft-tissues that will be present in *in vivo* animal and clinical experiments. The frequency was chosen to optimize trade-off between attenuation and focal dimensions. The transducer was fixed in place. The vertebrae were clamped at the anterior edge of the vertebral body, and positioned using a manual 3-axis positioning system such that the geometric focus of the transducer was at the centre of the vertebral foramen. These transducer-vertebra configurations are shown in Fig. 1a.

Five sets of measurements were made in each position shown in Fig. 1a), for each even numbered thoracic vertebra (T2, T4, ...T12). The first set of measurements for each position was performed with the transducer beam intersecting the superior component of the posterior arch, then the vertebrae were shifted by 2.5 mm along the vertical axis (z-axis, Fig. 1c) between each set of measurements using a stage micrometer. This corresponds to moving the transducer in the inferior direction. A total of 90 unique transducer-vertebra configurations were tested (15 per vertebra).

The coordinate system of the experiment was defined by the stationary transducer. The x-axis corresponds to the axis of the transducer, and the yz-plane corresponds to the the face of the transducer. The origin (0,0,0) was defined as the geometric focus of the transducer, and remained the same regardless of vertebra position. When the vertebra is in position 1 as shown in Fig. 1a, the x-axis corresponds to the anterior-posterior axis, the y-axis corresponds to the horizontal axis, and the z-axis corresponds to the vertical axis, as shown in Fig. 1c. The vertebrae were positioned such that the superior and inferior faces of the vertebral bodies were aligned with the xy-plane.

The transducer was driven with a single cycle pulse (Pulse Repetition Frequency:

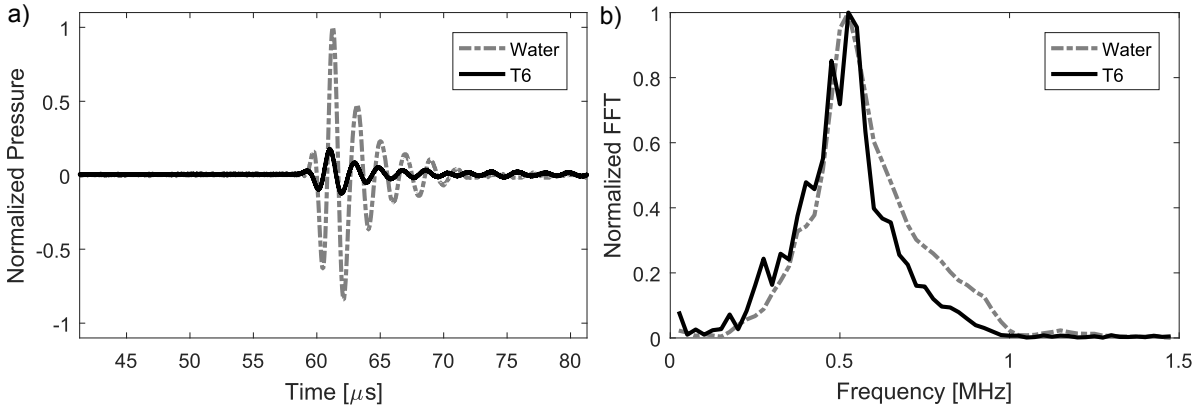

Figure 2. The transducer is excited with a single cycle pulse. a) The resultant time domain pressure profile at the transducer geometric focus in water, and in the sixth thoracic vertebra foramen (T6). The waveforms are normalized by the maximum water pressure amplitude. b) The corresponding frequency spectrum for each time domain signal, self-normalized to facilitate comparison.

1kHz, Function Generator: Tektronix AFG3052C, Amplifier: NP Technologies model NP-2519) at an amplitude below the threshold of non-linear effects. This pulse is chosen to negate the need for modeling multiple reflections within the vertebral canal; a task for which Ray Acoustics is ill-suited [42]. An example of time domain pressure at the transducer geometric focus is shown for water and the vertebral foramen in Figure 2.

A needle hydrophone (Precision Acoustics, 0.5mm diameter), oscilloscope (Tektronix MDO3014), and electronic three-axis positioning system (VelMex) were used to measure the pressure field within the vertebral foramen at a sampling rate of 40 MS·s^{-1}. The hydrophone was aligned with the z-axis, with the tip of the hydrophone facing in the positive direction to allow pressure measurements to be made in the vertebral foramen. The positioning system was used to measure pressure waveforms in 8 x 8 x 8 mm^3 volumes and 10 x 10 mm^2 yz-slices centered at the geometric focus of the transducer within the vertebral foramen. The step size for the volume scan was 0.5 mm, and the step size for the planar scans was 0.2 mm. Scan dimensions were constrained by the geometry of the vertebral foramen, and step size was constrained by experiment time. Volume measurements were completed for voxel-wise comparison between experiment and simulation, and the planar scans for a higher resolution comparison of focal distortion at the geometric focus of the transducer. The needle hydrophone tip was used to record the position of nine anatomical markers on the superior vertebra surface for each vertebra position shown in Fig. 1a), for each tested vertebra. These positions were recorded for the purpose of generating the affine transformation required for later registration of the simulation space to the experiment space [43].

A singular set of measurements was performed with T5 to test the ratio of maximum transmitted pressure within the vertebral foramen to the maximum pressure reflected from the lamina surface. T5 was positioned according to Position 3 Fig.1a. Pressure measurements were first performed in an 8 x 8 x 8 mm^3 volume centered at the origin

in water. Then, T5 was inserted. Pressure measurements were then performed in an identical 8 x 8 x 8 mm^3 volume centered at the origin to determine transmission pressure, and an 8 x 8 x 8 mm^3 volume centered at (18,0,0) mm was performed to determine reflected pressure. The position of the volume centered at (18,0,0) mm was chosen because $x = 14$ mm was the closest the hydrophone could be brought to the lamina surface without touching.

2.2. Transvertebral Ultrasound Propagation Model

Transvertebral ultrasound propagation was modelled using ray acoustics; a simulation method based on the Rayleigh-Sommerfeld integral used to calculate sound fields based on the point source response of a homogeneous fluid (Equation 1):

$$\Psi = \frac{1}{2\pi} \iint_S u \frac{e^{-j\mathrm{k}r}}{r} ds \tag{1}$$

where Ψ is the acoustic velocity potential, r is the distance between the source and point of interest, and the normal component of the surface velocity of the transducer is denoted u. The velocity u contains the time dependence of the source, $e^{-j\omega t}$. Wavenumber is defined as $\mathrm{k} = \omega/c$, where ω is angular frequency and c is the speed of sound in the medium. The velocity potential at a point is determined by integrating over the surface S [22]. The method introduced by O'Neil was extended to acoustic field calculations in inhomogeneous fluids with flat and curved interfaces, and later to flat and curved fluid-solid and solid-fluid interfaces [24, 25]. This is accomplished by discretizing the Rayleigh-Sommerfeld integral and treating the source and interface as separate meshes. Sound is propagated from every source mesh element to every interface mesh element using the Rayleigh-Sommerfeld integral and appropriate transmission and reflection coefficients [23]. The interface elements are then treated as a new hemispherical sources of transmitted (propagating in the direction of the interface element normal) and reflected (propagating in the opposite direction of the interface element normal) longitudinal and shear (when appropriate) waves. These steps are repeated to propagate sound across a series of interfaces. This method has been described in the literature, and White 2006 [27] treats the physics of ultrasound propagation from a source to a fluid-solid interface, then to a solid-fluid interface. The ray acoustics method for curved interfaces has been applied to focusing across soft tissue interfaces [24, 25, 44, 45, 46, 47], and used for early simulations of trans-skull ultrasound propagation [48, 16, 28, 29]. This article describes the application of Ray Acoustics simulation to modelling transvertebral ultrasound propagation.

Ray acoustics simulation accuracy depends on accurate mesh representation of the vertebral surfaces. The following method was used to generate mesh representations of the vertebrae from the CT scans described in section 2.1. Semi-automatic segmentation was performed in an open source program called ITK-SNAP to generate 3D binary masks representing the individual vertebrae [49]. This process involved manually

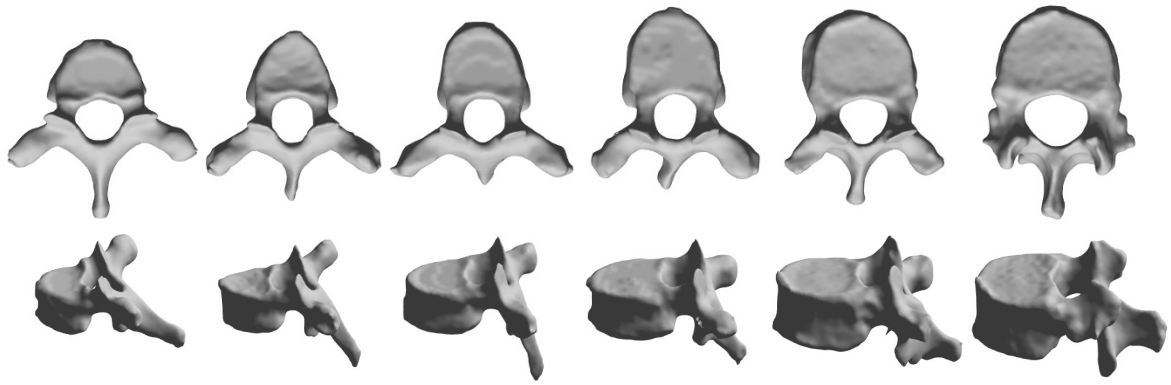

Figure 3. Mesh representations of even-numbered thoracic vertebrae, from left to right: T2, T4, T6, T8, T10, and T12. Superior (top row) and lateral (bottom row) perspectives.

choosing initialization points within the vertebrae followed by automatic active contour evolution. An open source mesh generating algorithm (ISO2MESH) was then used to generate a mesh representations of the vertebrae using the binary masks [50]. The mesh representations of the even-numbered thoracic vertebrae are displayed in Fig. 3. A mesh discretization study was performed to determine optimal mesh element area to maximize ray acoustics simulation accuracy without incurring significant computational penalty. Interface power convergence within 0.5% was found to occur with a maximum mesh element area of $(\lambda/6)^2$. The transducer was discretized with a uniform mesh element area of $(\lambda/12)^2$.

Mode conversion at fluid-solid interfaces was included in the ray acoustics model, as it has been shown that shear mode propagation contributes significantly to the transmitted pressure through skull at non-normal incident angles [26, 27, 28]. This is particularly relevant for vertebrae, as the irregularity of the posterior vertebra surface dictates that ultrasound propagating from a regular surface (e.g. spherically focused transducer, flat phased array) will intercept the posterior elements of the vertebra at non-normal angles.

Spatially heterogeneous acoustic properties were added to the model by correlating CT intensity to longitudinal acoustic properties [32, 10, 33]. CT density is calculated for each voxel using a linear function of CT intensity, $\rho = a \cdot HU + b$, where the parameters a and b are calculated from the voxel Hounsfield intensity (HU) and densities of water and air. Frequency dependent acoustic parameters are then interpolated from previously determined relationships from skull bone [10, 33]. Path-average acoustic properties (shear and longitudinal speed of sound and attenuation) are calculated for each source - target pair of elements from the voxels encountered along the ray path. Local acoustic properties (shear and longitudinal speed of sound, density) are calculated at target elements to determine transmission/reflection coefficients from the bone voxels nearest to the target element.

A binary mask-based occlusion test was added to the model to approximately model

ultrasound propagation past a finite interface. This is necessary for a ray acoustics simulation in single vertebrae, where sound may propagate directly from part of the transducer surface to a point of interest, but sound from the remainder of the surface must propagate through the vertebra using the fluid-solid $\rightarrow$ solid-fluid ray acoustics model. The occlusion test is applied when propagating ultrasound from the transducer to the vertebra (fluid = $true$, solid = $false$), when propagating ultrasound through the vertebra (fluid = $false$, solid = $true$), and when propagating ultrasound from all meshes to a point of interest in the fluid (fluid = $true$, solid = $false$). The test propagates voxel-by-voxel along the path between source and target. A path is considered occluded if a $false$ voxel was encountered along the path, and all nearest neighbours of the $false$ voxel were also false. In this case, the test ends. The occlusion test adds computational cost, but is necessary for simulations of ultrasound propagation past finite interfaces. The ray acoustics simulation was performed using an NVIDIA GeForce GTX 1060 6GB GPU with simulation times for a given transducer-vertebra configuration less than ten minutes for vertebral mesh discretization of $(\lambda/12)^2$, and less than 30 s for vertebral mesh discretization of $(\lambda/6)^2$. Given that the ray acoustics simulation is easily parallelizable, multiple GPUs could be used to further decrease computation time relative to full-wave simulations. To date, there are no reports on the computational cost for simulating transvertebral ultrasound propagation with a full-wave acoustic model, however full-wave transskull ultrasound propagation models that treat skull as solid reportedly take over 60 hours [51, 34], approximately three orders of magnitude longer than ray acoustics simulation. The lesser computational cost of the ray acoustics model will be particularly advantageous for *in situ* beamforming, crucial for clinical translation of ultrasound beamforming through vertebrae.

The corresponding positions of the nine anatomical markers measured in experiment space were measured in simulation space using the mesh representations of the vertebrae. The optimal affine transformation [43] for simulation registration to the experiment setup was applied for each transducer-vertebra configuration described in section 2.1, and a ray acoustics simulation was performed to generate pressure calculations in the exact yz-slices and xyz-volumes of the pressure measurements. Simulation pressure magnitudes were used for comparison with experimental results.

3. Results

Simulation accuracy was quantified through comparison of simulated pressure profiles with experimentally measured pressure profiles. Sets of experimental measurements were performed for a total of ninety transducer-vertebra configurations, split evenly among even-numbered thoracic vertebrae, and further split evenly among the three positions displayed in Fig. 1a. Corresponding ray acoustics simulations were completed for each transducer-vertebra configuration, and Fig. 4 displays five examples for experimentally measured and simulated pressure profiles for ultrasound propagation through T12 for comparison, and as an example of highly distorted foci due to

transvertebral ultrasound propagation. Three methods of quantitative comparison

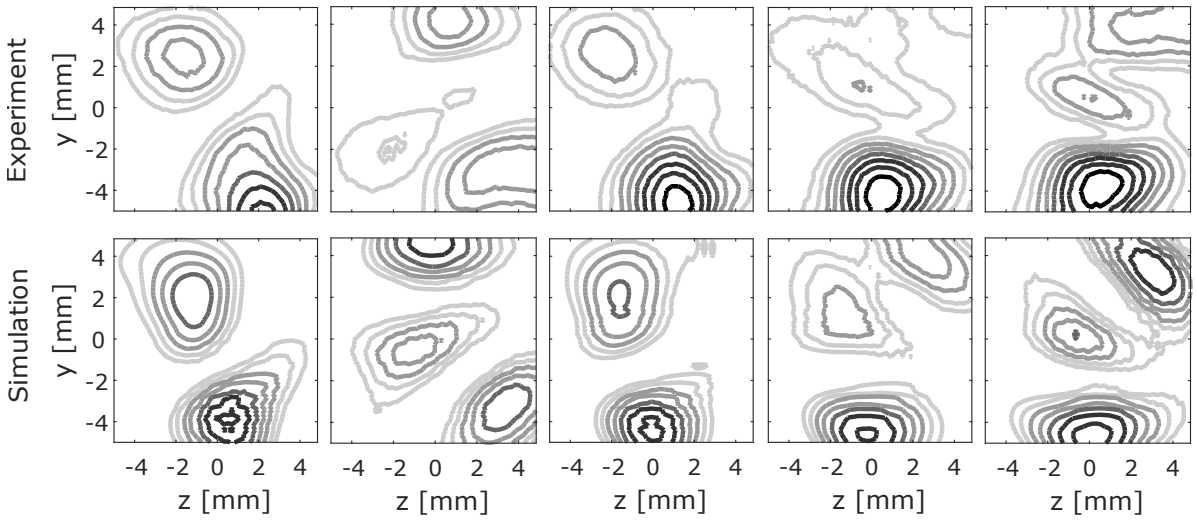

Figure 4. Transmitted pressure contour maps, normalized to the focal pressure in water. Contour lines indicate 10%-30% in 2.5% increments for experimentally measured and corresponding simulated transmitted pressure through the right lamina of the twelfth thoracic vertebra (T12). The vertebra was translated by 2.5 mm in the z-direction (See Fig. 1c) between scans.

between experimentally measured and simulated transvertebral ultrasound propagation are reported in the following subsections. The first is insertion loss, intended to measure the accuracy of the ray acoustics method in accounting for reflective losses and attenuation. The second metric is voxel pressure error, which measures similar attributes to insertion loss but includes a greater degree of spatial information. The final method is through comparison of focal distortion, solely a measure of spatial information. These three methods are intended to measure the accuracy and applicability of both the extension of skull acoustic parameters to vertebral bone and the extension of ray acoustics to transvertebral ultrasound propagation. All analysis was performed in Matlab 2016b.

3.1. Insertion Loss: Experiment vs. Simulation

Figure 5 reports maximum transmitted pressure measured in experiment and maximum simulated transmitted pressure for each transducer-vertebra configuration. Experiment and simulation pressures are normalized by maximum pressure in a water-only case. The maximum simulation pressures are calculated in the same 8 x 8 x 8 mm^3 volumes centered at the origin as those measured experimentally, and the maximum simulation pressures are normalized by the calculated pressure at the origin, again without the presence of the vertebra.

Table 1 reports the mean and standard deviation in the maximum normalized transmitted pressure in the vertebral canals of the tested vertebra-transducer configurations. Table 1 also reports the mean and standard deviation in simulation

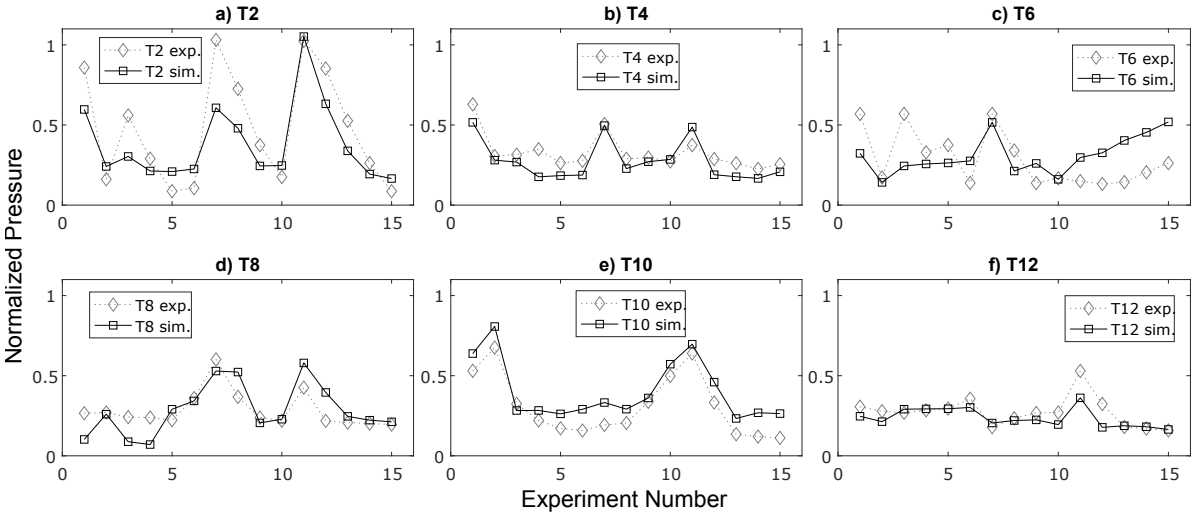

Figure 5. Maximum experimentally measured (red) and simulated (black) transmitted pressure for fifteen transducer-vertebra configurations per vertebra. Experiment numbers 1-5, 6-10, and 11-15 correspond to vertebra positions 1, 2, and 3, respectively (see Fig. 1a). The vertebra was shifted in the vertical direction by 2.5 mm between experiments, within each set of five experiments.

error in predicting these maximum pressures. Table 1 can be used to calculate average insertion loss by vertebra.

	T2	T4	T6	T8	T10	T12	Total
μ_{exp} [%]	38.3	27.5	31.0	28.6	40.3	23.7	31.6
σ_{exp} [%]	±24.6	± 12.3	±11.6	±16.0	±18.6	±5.8	±16.6
μ_{error} [%]	-9.1	-5.2	2.6	0.2	9.3	-3.6	-0.9
σ_{error} [%]	±17.1	±6.4	±18.6	±11.1	±5.3	±6.0	±13.1

Table 1. Mean (μ_{exp}) and standard deviation (σ_{exp}) in experimentally measured maximum transmitted pressure in the vertebral canal. Mean error (μ_{error}) and standard deviation σ_{error} simulation error (experiment - simulation) in predicting maximum transmitted pressure in the vertebral canal. Pressures are normalized. 15 unique transducer-vertebra configurations were tested per vertebra.

3.2. Voxel Pressure: Experiment vs. Simulation

Voxel pressure error was chosen as an exact measure of the difference between experiment and simulation, although this method suffers in relaying information about the spatial differences between experiment and simulation. Total mean voxel pressure error (p^{err}_{mean}, Eq. 2), standard deviation in voxel pressure error ($p^{\text{err}}_{\text{SD}}$, Eq. 3), root-mean-square voxel pressure error (p_{RMS}, Eq. 4), and cross-correlation between experiment and simulation (p_{xc}, Eq. 5) is reported in Table 2 by vertebra. p_{RMS} and p_{xc} are commonly used global similarity measures with spatial alignment, while p^{err}_{mean} and $p^{\text{err}}_{\text{SD}}$ provide insight into the

origin of the p_{RMS} and p_{xc} values. [52, 53].

$$p_{mean}^{\mathrm{err}} = \frac{1}{N}\sum_{i=1}^{N}(p_i^{\mathrm{exp}} - p_i^{\mathrm{sim}}) \tag{2}$$

$$p_{\mathrm{SD}}^{\mathrm{err}} = \sqrt{\frac{1}{N}\sum_{i=1}^{N}(p_i^{\mathrm{exp}} - p_i^{\mathrm{sim}} - p_{mean}^{\mathrm{err}})^2} \tag{3}$$

$$p_{\mathrm{RMS}} = \sqrt{\frac{1}{N}\sum_{i=1}^{N}(p_i^{\mathrm{exp}} - p_i^{\mathrm{sim}})^2} \tag{4}$$

$$p_{\mathrm{XC}} = \frac{\sum_{i=0}^{N} p_i^{\mathrm{exp}} p_i^{\mathrm{sim}}}{\sqrt{\sum_{i=0}^{N}(p_i^{\mathrm{exp}})^2 \sum_{i=0}^{N}(p_i^{\mathrm{sim}})^2}} \tag{5}$$

In equations 2-5, N is the number of voxels compared, and p_i^{exp} and p_i^{sim} is the pressure of the i^{th} voxel measured experimentally and calculated using Ray Acoustics respectively. In this table, voxel error is combined for all measured voxels per volume ($N_{voxels} = 18^3$), and all vertebra-transducer configurations ($N = N_{scans}N_{voxels} = 15 \times 18^3$). The image similarity metrics are reported for measured and simulated pressure in an 8 x 8 x 8 mm^3 volume in water for comparison.

	Water	T2	T4	T6	T8	T10	T12	Total
p_{mean}^{err} [%]	3.63	1.63	-1.37	2.79	0.72	3.80	-0.34	1.21
$p_{\mathrm{SD}}^{\mathrm{err}}$ [%]	±6.96	±9.31	±5.39	±8.90	±5.47	±5.23	±4.66	±7.07
p_{RMS} [%]	7.85	9.45	5.56	9.40	5.51	6.46	4.67	7.17
p_{XC} [%]	98.0	86.0	91.2	71.8	88.3	93.8	92.0	87.2

Table 2. Total mean voxel pressure error (p_{mean}^{err}), standard deviation in voxel pressure error $p_{\mathrm{SD}}^{\mathrm{err}}$, root-mean-square voxel pressure error p_{RMS}, and cross-correlation between experiment and simulation pressure (p_{XC}) in predicting pressure in an 8 x 8 x 8 mm^3 volumes centered at the geometric focus of the transducer for fifteen unique transducer-vertebra configurations per tested vertebra. These metrics are also displayed for an identical volume with no vertebra, and labelled 'water'.

3.3. Focal Distortion: Experiment vs. Simulation

The accuracy of the Ray Acoustics method for predicting focal distortions was quantified using two metrics: error in predicting focal maximum (I_{max}) location (y_{max}, z_{max}), and error in predicting weighted focal volume (I_{vol}) location (y_{vol}, z_{vol}), defined by Eq. 6.

$$(y_{vol}, z_{vol}) = \left(\frac{\sum I(y_i, z_i)y_i}{\sum I(y_i, z_i)}, \frac{\sum I(y_i, z_i)z_i}{\sum I(y_i, z_i)}\right) \tag{6}$$

where $I(y_i, z_i) \geq 0.5I_{max}$ to restrict the weighting to values greater than 50% of I_{max}. These metrics are termed I_{max} and I_{vol} as they represent the location of the point

maximum and the location of the centre of the focal volumetric distribution. These metrics were evaluated using the two-dimensional yz scans, as the depth-of-field of the transducer is approximately 30 mm, resulting in a slowly varying pressure profile in the x-direction, biasing three-dimensional error measurements towards over-reporting error in the x-axis. The spherical symmetry of the transducer removes bias between y and z for the pressure profile in water, however, the presence of a vertebra introduces focal shifts and distortions that are systematically different in y and z. For this reason, error in Max and Vol are reported in y ($y_{err} = y_{exp} - y_{sim}$) and z ($z_{err} = z_{exp} - z_{sim}$) separately, and also reported as an absolute error ($r_{err} = (y_{err}^2 + z_{err}^2)^{1/2}$ in the yz-plane. y_{err} and z_{err} are represented by Matlab boxplots, where the central mark indicates median, the bottom and top marks represent 25th and 75th percentile, whiskers represent the most extreme data points not considered outliers, and outliers are plotted as red '+' symbols.

Error in I_{max} indicates the ability of the Ray Acoustics method to correctly predict the location of maximum signal phase coherence and signal strength. Error in I_{vol} provides a more accurate representation of error in predicting the location of bioeffects, and for better comparison of focii that are distorted, especially if a focus is spatially split, and the simulation predicts the wrong sub-focus as I_{max}.

Figure 6 displays simulation error for all combined results: 15 measurements and simulations per even-numbered thoracic vertebra, five focusing through the posterior arch, five focusing through the left lamina, and five focusing through the right lamina, totalling 90 measurements and simulations. Figure 6a) displays the distributions of simulation error in I_{max} and I_{vol} in the horizontal (y) and vertical (z) directions, and Figure 6b) displays the distribution of absolute simulation errors in the frontal (yz) plane. Mean ± standard deviations in simulation error in predicting I_{max} and I_{vol} were ($y_{err} = -0.37 \pm 1.8$ mm, $z_{err} = 0.08 \pm 2.5$ mm) and ($y_{err} = -0.19 \pm 0.9$ mm, $z_{err} = 0.24 \pm 1.6$ mm), respectively. Mean absolute simulation error (r_{err}) in predicting I_{max} and I_{vol} was 2.3 mm and 1.5 mm, respectively.

Figures 7 and 8 display the data reported in Fig. 6, separated by vertebra. Mean and standard deviation of simulation error in 'Max' and 'Vol' are reported in Table 3.

Error	T2 [mm]	T4 [mm]	T6 [mm]	T8 [mm]	T10 [mm]	T12 [mm]	Total
$y_{\max}$	-0.38 ± 1.31	-0.01 ± 1.08	-0.58 ± 1.89	0.19 ± 0.77	0.03 ± 0.85	-1.50 ± 3.20	-0.42 ± 1.77
y_{vol}	-0.21 ± 0.58	-0.04 ± 0.81	-0.04 ± 0.76	0.16 ± 0.61	0.07 ± 0.70	-1.11 ± 1.10	-0.22 ± 0.85
$z_{\max}$	0.87 ± 3.38	-0.50 ± 1.36	0.81 ± 2.98	-1.35 ± 1.93	-0.04 ± 2.20	0.71 ± 2.26	0.14 ± 2.53
z_{vol}	0.98 ± 2.20	-0.29 ± 1.19	0.46 ± 1.99	-0.38 ± 0.84	0.54 ± 1.23	0.15 ± 1.16	0.31 ± 1.61
$r_{\max}$	3.01	1.45	2.83	1.63	1.76	3.05	2.34
r_{vol}	1.82	1.31	1.75	0.97	1.29	1.65	1.51

Table 3. Simulation error by vertebra, for all transducer-vertebra configurations. Reported simulation errors are in focal maximum location ($y_{\max}, z_{\max}, r_{\max}$) and weighted focal volume location ($y_{\text{vol}}, z_{\text{vol}}, r_{\text{vol}}$).

Five measurements and simulations per even-numbered thoracic vertebra were performed with the transducer focused through the posterior arch of the vertebra (Fig. 1a), totalling thirty measurements and simulations. Mean ± standard deviations

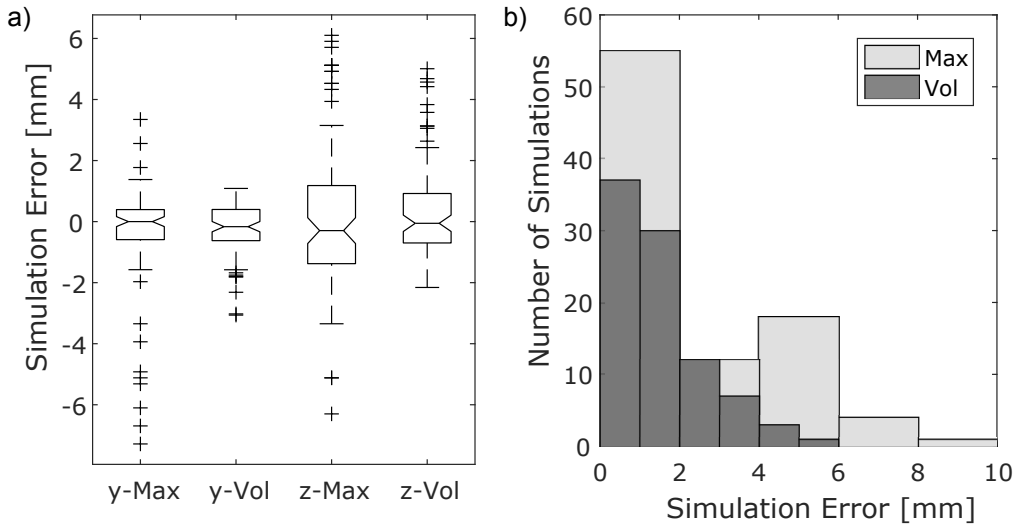

Figure 6. Simulation error for all 90 tested transducer-vertebra configurations and respective simulations. a) Simulation error in focal maximum ('Max') location and weighted focal volume ('Vol) location is reported using boxplots for y_{err} (error horizontal axis), z_{err} (error vertical axis). b) Distribution of absolute simulation errors in 'Max' and 'Vol' in the frontal plane.

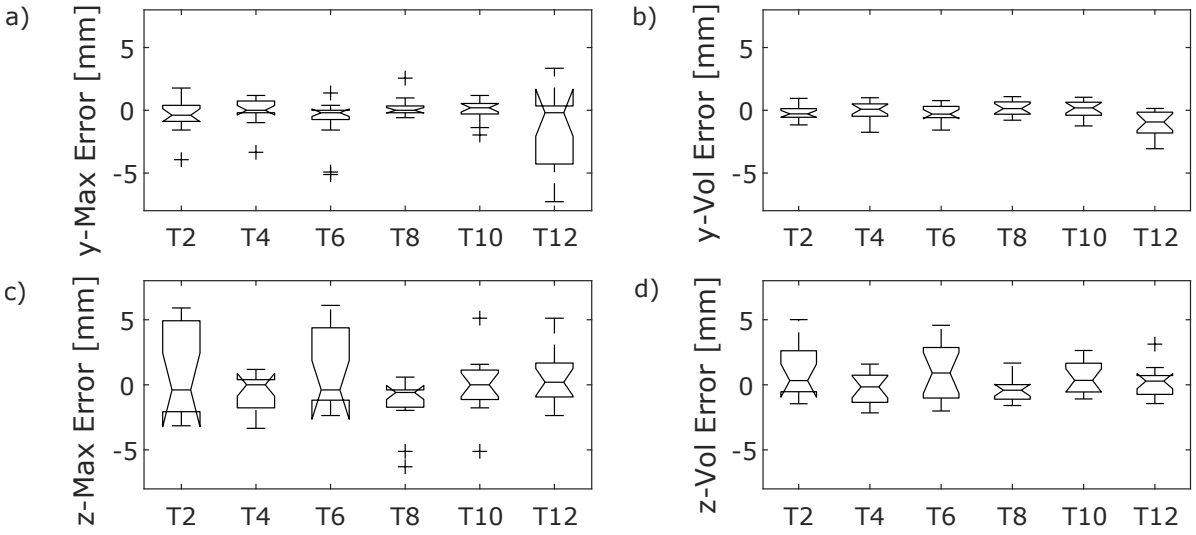

Figure 7. Simulation error for the 15 tested transducer-vertebra configurations per vertebra. Simulation error in focal maximum ('Max') location and weighted focal volume ('Vol) location is reported using boxplots for y_{err} (error horizontal axis) in plots a) and b), z_{err} (error vertical axis) in plots c) and d).

in simulation error in predicting I_{max} and I_{vol} were ($y_{err} = -0.6 \pm 1.4\,\text{mm}$, $z_{err} = 0.1 \pm 2.2\,\text{mm}$) and ($z_{err} = -0.3 \pm 0.7\,\text{mm}$, $z_{err} = 0.3 \pm 1.5\,\text{mm}$) respectively. Mean absolute simulation error (r_{err}) in predicting I_{max} and I_{vol} was 1.9 mm and 1.4 mm, respectively. Five measurements and simulations per even-numbered thoracic vertebra were performed for both left and right lamina of the vertebra: ten measurements and

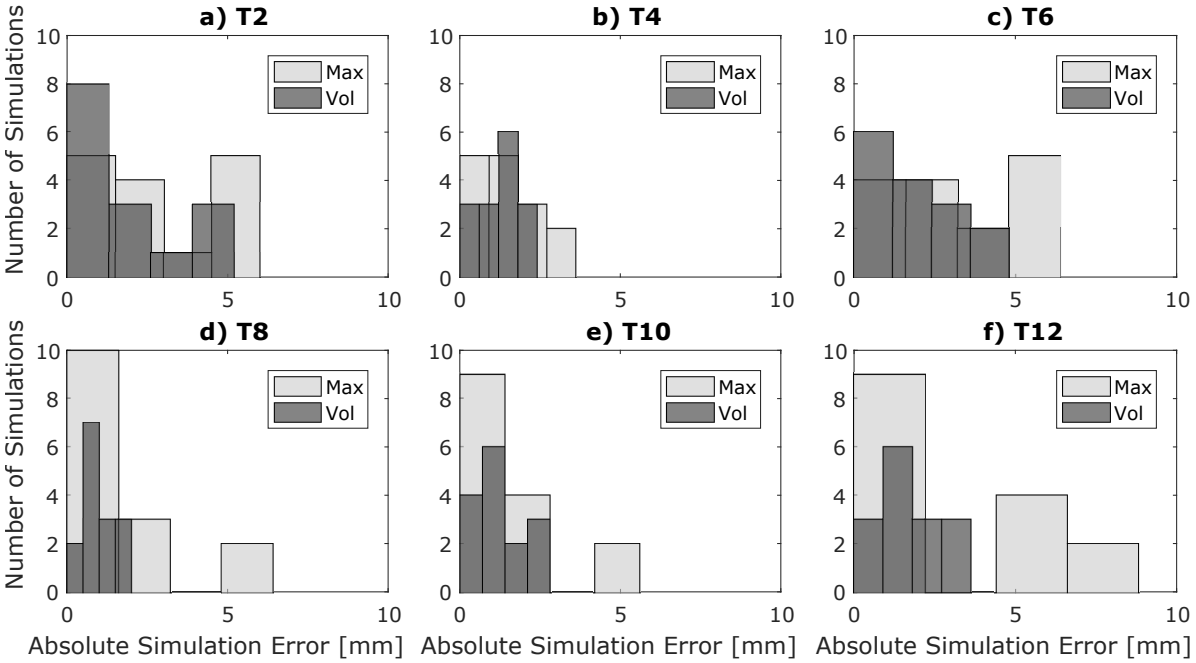

Figure 8. Absolute simulation error for the 15 tested transducer-vertebra configurations per vertebra. Reported simulation errors are in absolute focal maximum ('Max') location and absolute weighted focal volume ('Vol) location in the frontal (yz) plane.

simulations per even-numbered thoracic vertebra, totalling sixty measurements and simulations. Mean ± standard deviations in simulation error in predicting I_{max} and I_{vol} were ($y_{err} = -0.3 \pm 1.9\,\text{mm}$, $z_{err} = 0.2 \pm 2.7\,\text{mm}$) and ($y_{err} = -0.2 \pm 0.9\,\text{mm}$, $z_{err} = 0.3 \pm 1.7\,\text{mm}$) respectively. Mean absolute simulation error (r_{err}) in predicting I_{max} and I_{vol} was 2.6 mm and 1.6 mm, respectively.

3.4. Focal vs. Pre-laminar Pressure

Figure 9 displays experimentally measured and simulated yz-slices from 8 x 8 x 8 mm^3 volume scans in water, in the vertebral canal of the fifth thoracic vertebra, and in the pre-laminar region of the fifth thoracic vertebra. The maximum experimentally measured normalized pressures in the canal and in the pre-laminar region were 0.33 and 0.6, respectively, giving an experimental canal / pre-laminar pressure ratio of 0.55. The maximum simulated normalized pressures in the canal and in the pre-laminar region were 0.22 and 0.46, respectively, giving a simulated canal / pre-laminar pressure ratio of 0.48.

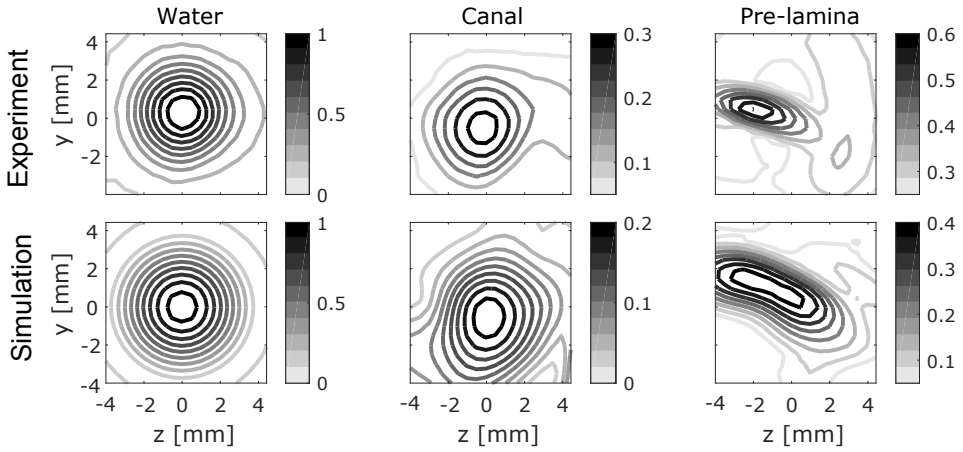

Figure 9. Normalized pressure contour maps for experimentally measured and corresponding simulated focii in water, at the centre of the canal of the fifth thoracic vertebra (T5), and in the maximum pressure plane in the pre-laminar region. T5 was oriented such that the transducer was focused through the left lamina (Position 3, Fig.1)

4. Discussion

There are several sources of error that must be considered when evaluating the accuracy of a heterogeneous ray acoustics model with acoustic properties derived from skull bone for simulating transvertebral ultrasound propagation. One source of error is in the image registration process. The average absolute distance between experimentally measured control point and registered simulation control point was 1.3 mm. Nine control points were used per vertebra-transducer configuration, and it is expected that error per control point results in a total registration error relative to ground truth to be smaller than 1.3 mm. Registration error of this magnitude is relevant in terms of vertebra rotation, as transmission and reflection is highly dependent on angle of incidence (e.g Cobbold Fig 1.20 [54]).

Needle hydrophone orientation was another source of experiment error. An increase of 20% in sensitivity has been recorded when the hydrophone is aligned $+x$ axis, versus the orientation used in the reported experiments, where the hydrophone is aligned with the $+z$ axis. The orientation dependence of the needle hydrophone results in higher recorded pressures when the angle between an incoming ultrasound wavefront and the hydrophone decreases. This effect is seen as a small distortion in the recorded water pressure profile displayed in Fig. 9. Needle hydrophone orientation partially accounts for the error in simulated voxel pressure for the water-only case, shown in Table 2. The remainder of the error in simulated voxel pressure for the water-only case is experiment noise, seen in Fig. 9 as the shallower pressure gradient away from the focus in experiment relative to simulation.

Short pulses were used in experiment to remove the need to model multiple reflections and the resultant standing waves within the vertebral canal. The ray acoustics

method assumes a steady-state solution and a mono-frequency source. Short pulses introduce higher frequency content, which undergoes velocity dispersion and frequency-dependent attenuation when propagating through bone [55, 56, 10, 33]. However, these effects are not expected to cause significant simulation error, inferring from the minor change in pulse frequency spectrum due to propagating through bone shown in Fig. 2. The advantages of pulsed wave ultrasound include being an ideal method for preventing the formation of hard-to-control standing waves [57, 58], and ray acoustics provides an appropriate first-order approximation for pulsed ultrasound propagation through vertebral bone without incurring the large computational penalty of a full-wave model.

The results reported for experimental insertion loss, and the corresponding simulated insertion losses are interesting from both experiment and simulation perspectives. Figure 5 demonstrates that the transmitted pressure and corresponding insertion loss is highly dependent on transducer-vertebra configuration. Mean experimentally measured transmission through the vertebrae was 31.6% transmission, similar to reported losses due to propagating through skull [35]. In some of the tested transducer-vertebra configurations (e.g. T2) a substantial amount of sound was directly transmitted from transducer to hydrophone, without intercepting the vertebra. This effect is pronounced in T2 due to the limited vertical dimension of T2 (see Fig. 3), and given that experimental protocol dictated that the transducer be translated a total of 10 mm in z between experiments 1 and 5, 6 and 10, 11 and 15. In one case (T2, experiment 11) this resulted in a normalized pressure greater than one. In this case the reflective surface of the vertebra redirects ultrasound towards the measurement plane, resulting in the measured and simulated pressure with the vertebra in plane being higher than without the vertebra. This is relevant for stacked vertebrae, where interlaminar spaces between vertebrae may provide an opportunity for delivering ultrasound to the spinal cord without significant focal aberration and without significant reflective and attenuative losses.

Figure 5 and table 1 show that simulated transmission trends matched well in T4, T8, T10, T12, not as well in T2, and poorly in T6. The image similarity metrics reported in table 2 reflect this finding. Table 2 shows that average p_{RMS} in vertebrae is within 1% of p_{RMS} in water, although average experiment-simulation cross-correlation p_{XC} is 87.2%, less than that of water (98%). This is an intuitive finding, given that simulation error in the vertebra-induced distortions (table 3) will result in a lesser degree of cross-correlation than the water case, where focal distortion in the plane of the transducer is effectively zero.

In all tested vertebrae save T6, simulation predicts insertion loss more accurately than mean insertion loss. This trend is reflected in the reported image similarity metrics, and in $r_{\max}$ and r_{vol} reported in table 3. The registration error per registered control point was 1.3 mm and 1.1 mm for T2 and T6 respectively, although there may have been unaccounted bias in the measurement of the control points given the lack of ground truth registration. T2 has a spinous process that projects in the posterior direction (Fig. 3), and in nine out of fifteen simulated cases, the shear/longitudinal transmitted power

ratio at the water-bone interface was greater than 10. In this case, a more natural model for combined shear and longitudinal ultrasound propagation such as a full-wave model based on the viscoelastic wave equation may be more appropriate [33], or a hybrid model that combines ray acoustics with a full-wave model [42, 59]. This does not explain the result for T6, which has a spinous process that projects in the caudal direction (Fig. 3), and with eleven out of fifteen simulated cases having a shear/longitudinal transmitted power ratio at the water-bone interface less than one. It is more likely that bias in the location or the control points resulted in the higher simulation errors for T6, and ruling out geometric dependence of the simulation errors could potentially be achieved by extending the existing data-set to the odd-numbered thoracic vertebrae, and to additional spines.

Figures 6 shows that for the entire dataset, there is a trend that simulation error in z exceeds simulation error in y. Two potential sources for this error have been discussed - hydrophone orientation, and rotation error of the registered simulation mesh around the y-axis, resulting in incorrect incident ultrasound angles at the water-bone interface. In general, the ray acoustics model did not appear to be biased towards directional error along the y and z axes, although a complete statistical analyses has not been performed. Figure 7 and 8 show that there are cases where the simulation model fails to predict I_{max} and I_{vol} by 5 mm or more, which is biologically meaningful when considering the 4.9 mm full-width half maximum of the transducer, the 10 mm diameter of the spinal cord, and the 15-20 mm diameter of the vertebral foramen [60, 41]. However, in the majority of cases, the location of I_{max} and I_{vol} is predicted within approximately 2 mm in the yz-plane, a reasonable tolerance given the dimensions of the spinal cord and considering registration error. Simulation accuracy is slightly worse when predicting ultrasound propagation through the vertebral laminae when compared to predicting ultrasound propagation through the posterior arch of the vertebra. This may be due to the presence of the transverse processes and multiple reflections (transducer $\rightarrow$ reflection from transverse process $\rightarrow$ transmission through lamina) that were not included in the model. Multiple reflections could be added to the ray acoustics model using an adaptation of the model to include directionality in the reflected sound to prevent unphysical backpropagation of sound in the model. As is, the ray acoustics model is able to model singular reflections, as shown in Fig. 9. This experiment was performed to obtain an idea of the ratio of maximum pressure within the canal to the maximum pressure in the pre-laminar region between transducer and vertebra, and the paired simulation shows that although the pressure magnitudes are lower than in experiment, the ratio is close to that observed in experiment. The experimental focal vs. pre-laminar pressure ratio of 0.55 highlights the need for caution to be taken when focusing ultrasound to the vertebral canal. However, this ratio may be significantly improved through the use of two transducers (one focusing through each lamina), through phase and amplitude correction [61], and by focusing through interlaminar spaces. As demonstrated in Fig. 9, ray acoustics is capable of simulating the reflected pressure profile, and may be a useful aid in predicting and preventing the formation of

foci from the reflected component of an ultrasound wavefront incident on a vertebra.

5. Conclusion

Ray acoustics has been applied to modelling ultrasound propagation through the posterior elements of thoracic vertebrae using acoustic properties originally derived from skull bone [32, 42, 33]. Comparison between experiment and simulation shows that simulation error is similar to error accrued in the experimental process, suggesting that pursuing transvertebral ultrasound beamforming using ray acoustics with skull acoustic properties is a worthwhile endeavour. Comparison of simulation accuracy with a full-wave model should be performed in the future to characterize cases where ray acoustics is sufficiently accurate to perform transvertebral ultrasound beamforming, and cases that require a full-wave model. Future development of the ray acoustics simulation will necessarily include stacked vertebrae, and likely require the addition of soft tissue layers in order to reach the final goal of performing *in vivo* transvertebral ultrasound beamforming for BSCB opening and improved targeted drug delivery to the spinal cord.

6. Acknowledgments

Support for this work was provided by the Natural Sciences and Engineering Research Council of Canada (NSERC) through their Discovery Grant program and through the Ontario Graduate Scholarship program.

7. References

[1] Viktor Bartanusz, Daniela Jezova, Betty Alajajian, and Murat Digicaylioglu. The blood–spinal cord barrier: morphology and clinical implications. *Annals of neurology*, 70(2):194–206, 2011.

[2] Meaghan A O'Reilly, Edward Jones, Ryan Mand Barrett, Anthony Schwab, Elizabeth Head, and Kullervo Hynynen. Investigation of the safety of focused ultrasound-induced blood-brain barrier opening in a natural canine model of aging. *Theranostics*, 7(14):3573, 2017.

[3] Alexandre Carpentier, Michael Canney, et al. Clinical trial of blood-brain barrier disruption by pulsed ultrasound. *Sci Transl Med*, 8(343):343re2, 2016.

[4] Charissa Poon, Dallan McMahon, and Kullervo Hynynen. Noninvasive and targeted delivery of therapeutics to the brain using focused ultrasound. *Neuropharmacology*, 120:20–37, 2017.

[5] Yuexi Huang, Ryan Alkins, et al. Initial experience in a pilot study of blood-brain barrier opening for chemo-drug delivery to brain tumors by mr-guided focused ultrasound. *ISMRM 24th Annual Meeting & Exhibition*, 2016.

[6] Jeff Wachsmuth, Rajiv Chopra, and Kullervo Hynynen. Feasibility of transient image-guided blood-spinal cord barrier disruption. *8th International Symposium on Therapeutic Ultrasound*, 2009.

[7] Danielle Weber-Adrian, Emmanuel Thévenot, Meaghan A O'Reilly, et al. Gene delivery to the spinal cord using mri-guided focused ultrasound. *Gene therapy*, 22(7):568–577, 2015.

[8] Allison H Payne, Gregory W Hawryluk, Yoshimi Anzai, Henrik Odéen, Megan A Ostlie, Ethan C Reichert, Amanda J Stump, Satoshi Minoshima, and Donna J Cross. Magnetic resonance imaging-guided focused ultrasound to increase localized blood-spinal cord barrier permeability. *Neural regeneration research*, 12(12):2045, 2017.

[9] P. H. F. Nicholson, M. J. Haddaway, and M. W. J. Davie. The dependence of ultrasonic properties on orientation in human vertebral bone. *Physics in medicine and biology*, 39(6):1013–1024, 1994.

[10] Samuel Pichardo, Vivian W Sin, and Kullervo Hynynen. Multi-frequency characterization of the speed of sound and attenuation coefficient for longitudinal transmission of freshly excised human skulls. *Physics in medicine and biology*, 56(1):219–250, 2010.

[11] DJ Phillips, SW Smith, OT Von Ramm, and FL Thurstone. Sampled aperture techniques applied to b-mode echoencephalography. In *Acoustical Holography*, pages 103–120. Springer, 1975.

[12] Kullervo Hynynen and Ferenc A Jolesz. Demonstration of potential noninvasive ultrasound brain therapy through an intact skull. *Ultrasound in medicine & biology*, 24(2):275–283, 1998.

[13] Mickaël Tanter, Jean-Louis Thomas, and Mathias Fink. Time reversal and the inverse filter. *The Journal of the Acoustical Society of America*, 108(1):223–234, 2000.

[14] Greg T Clement and Kullervo Hynynen. Micro-receiver guided transcranial beam steering. *ieee transactions on ultrasonics, ferroelectrics, and frequency control*, 49(4):447–453, 2002.

[15] Kullervo Hynynen and J Sun. Trans-skull ultrasound therapy: The feasibility of using image-derived skull thickness information to correct the phase distortion. *IEEE transactions on ultrasonics, ferroelectrics, and frequency control*, 46(3):752–755, 1999.

[16] Greg T Clement and K Hynynen. A non-invasive method for focusing ultrasound through the human skull. *Physics in medicine and biology*, 47(8):1219, 2002.

[17] J-F Aubry, M Tanter, M Pernot, J-L Thomas, and M Fink. Experimental demonstration of noninvasive transskull adaptive focusing based on prior computed tomography scans. *The Journal of the Acoustical Society of America*, 113(1):84–93, 2003.

[18] Max Wintermark, Nicholas J Tustison, William J Elias, James T Patrie, Wenjun Xin, Nicholas Demartini, Matt Eames, Suna Sumer, Benison Lau, Alan Cupino, et al. T1-weighted mri as a substitute to ct for refocusing planning in mr-guided focused ultrasound. *Physics in Medicine & Biology*, 59(13):3599, 2014.

[19] G Wilson Miller, Matthew Eames, John Snell, and Jean-François Aubry. Ultrashort echo-time mri versus ct for skull aberration correction in mr-guided transcranial focused ultrasound: In vitro comparison on human calvaria. *Medical physics*, 42(5):2223–2233, 2015.

[20] Ryan M Jones and Kullervo Hynynen. Comparison of analytical and numerical approaches for ct-based aberration correction in transcranial passive acoustic imaging. *Physics in medicine and biology*, 61(1):23, 2015.

[21] Adamos Kyriakou, Esra Neufeld, Beat Werner, Margarethus Marius Paulides, Gabor Szekely, and Niels Kuster. A review of numerical and experimental compensation techniques for skull-induced phase aberrations in transcranial focused ultrasound. *International Journal of Hyperthermia*, 30(1):36–46, 2014.

[22] HoT O'Neil. Theory of focusing radiators. *The Journal of the Acoustical Society of America*, 21(5):516–526, 1949.

[23] Leonid M Brekhovskikh and Oleg A Godin. Plane-wave reflection from the boundaries of solids. In *Acoustics of Layered Media I*, pages 87–112. Springer, 1990.

[24] Xiaobing Fan and Kullervo Hynynen. The effect of wave reflection and refraction at soft tissue interfaces during ultrasound hyperthermia treatments. *The Journal of the Acoustical Society of America*, 91(3):1727–1736, 1992.

[25] Xiaobing Fan and Kullervo Hynynen. The effects of curved tissue layers on the power deposition patterns of therapeutic ultrasound beams. *Medical physics*, 21(1):25–34, 1994.

[26] Greg T Clement, P. Jason White, and K Hynynen. Enhanced ultrasound transmission through the human skull using shear mode conversion. *The Journal of the Acoustical Society of America*, 115(3):1356–1364, 2004.

[27] P. Jason White, Greg T Clement, and K Hynynen. Longitudinal and shear mode ultrasound propagation in human skull bone. *Ultrasound in medicine & biology*, 32(7):1085–1096, 2006.

[28] Samuel Pichardo and Kullervo Hynynen. Treatment of near-skull brain tissue with a focused device using shear-mode conversion: a numerical study. *Physics in medicine and biology*, 52(24):7313,

2007.

[29] Ryan M Jones, Meaghan A OReilly, and Kullervo Hynynen. Transcranial passive acoustic mapping with hemispherical sparse arrays using ct-based skull-specific aberration corrections: a simulation study. *Physics in medicine and biology*, 58(14):4981, 2013.

[30] Can Barış Top, P Jason White, and Nathan J McDannold. Nonthermal ablation of deep brain targets: a simulation study on a large animal model. *Medical physics*, 43(2):870–882, 2016.

[31] Elena A Kaye, Yoni Hertzberg, Michael Marx, Beat Werner, Gil Navon, Marc Levoy, and Kim Butts Pauly. Application of zernike polynomials towards accelerated adaptive focusing of transcranial high intensity focused ultrasound. *Medical physics*, 39(10):6254–6263, 2012.

[32] Christopher W Connor, Greg T Clement, and Kullervo Hynynen. A unified model for the speed of sound in cranial bone based on genetic algorithm optimization. *Physics in medicine and biology*, 47(22):3925, 2002.

[33] Samuel Pichardo, Carlos Moreno-Hernández, Robert Andrew Drainville, Vivian Sin, Laura Curiel, and Kullervo Hynynen. A viscoelastic model for the prediction of transcranial ultrasound propagation: application for the estimation of shear acoustic properties in the human skull. *Phys. Med. Biol*, 62:6938–6962, 2017.

[34] Laurent Marsac, Dorian Chauvet, Raphaël La Greca, A-L Boch, Kathia Chaumoitre, Mickael Tanter, and J-F Aubry. Ex vivo optimisation of a heterogeneous speed of sound model of the human skull for non-invasive transcranial focused ultrasound at 1 mhz. *International Journal of Hyperthermia*, 33(6):635–645, 2017.

[35] Francis J Fry and James E Barger. Acoustical properties of the human skull. *The Journal of the Acoustical Society of America*, 63(5):1576–1590, 1978.

[36] P Jason White, Sonali Palchaudhuri, Kullervo Hynynen, and Greg T Clement. The effects of desiccation on skull bone sound speed in porcine models. *ieee transactions on ultrasonics, ferroelectrics, and frequency control*, 54(8), 2007.

[37] Worawat Limthongkul, Eldin E Karaikovic, Jason W Savage, and Alexander Markovic. Volumetric analysis of thoracic and lumbar vertebral bodies. *The Spine Journal*, 10(2):153–158, 2010.

[38] Nir Lipsman, Michael L Schwartz, Yuexi Huang, Liesly Lee, Tejas Sankar, Martin Chapman, Kullervo Hynynen, and Andres M Lozano. Mr-guided focused ultrasound thalamotomy for essential tremor: a proof-of-concept study. *The Lancet Neurology*, 12(5):462–468, 2013.

[39] W Jeffrey Elias, Nir Lipsman, William G Ondo, Pejman Ghanouni, Young G Kim, Wonhee Lee, Michael Schwartz, Kullervo Hynynen, Andres M Lozano, Binit B Shah, et al. A randomized trial of focused ultrasound thalamotomy for essential tremor. *New England Journal of Medicine*, 375(8):730–739, 2016.

[40] Dan Dragomir-Daescu, Christina Salas, Susheil Uthamaraj, and Timothy Rossman. Quantitative computed tomography-based finite element analysis predictions of femoral strength and stiffness depend on computed tomography settings. *Journal of biomechanics*, 48(1):153–161, 2015.

[41] HY Ko, JH Park, YB Shin, and SY Baek. Gross quantitative measurements of spinal cord segments in human. *Spinal cord*, 42(1):35–40, 2004.

[42] Aki Pulkkinen, Yuexi Huang, Junho Song, and Kullervo Hynynen. Simulations and measurements of transcranial low-frequency ultrasound therapy: skull-base heating and effective area of treatment. *Physics in medicine and biology*, 56(15):4661, 2011.

[43] Berthold KP Horn, Hugh M Hilden, and Shahriar Negahdaripour. Closed-form solution of absolute orientation using orthonormal matrices. *JOSA A*, 5(7):1127–1135, 1986.

[44] Douglas R Daum and Kullervo Hynynen. A 256-element ultrasonic phased array system for the treatment of large volumes of deep seated tissue. *IEEE transactions on ultrasonics, ferroelectrics, and frequency control*, 46(5):1254–1268, 1999.

[45] Kathleen Mahoney, Todd Fjield, Nathan McDannold, Greg Clement, and Kullervo Hynynen. Comparison of modelled and observed in vivo temperature elevations induced by focused ultrasound: implications for treatment planning. *Physics in medicine and biology*, 46(7):1785, 2001.

[46] Nicholas Ellens, Aki Pulkkinen, Junho Song, and Kullervo Hynynen. The utility of sparse 2d fully electronically steerable focused ultrasound phased arrays for thermal surgery: a simulation study. *Physics in medicine and biology*, 56(15):4913, 2011.

[47] Nicholas Ellens and Kullervo Hynynen. Simulation study of the effects of near-and far-field heating during focused ultrasound uterine fibroid ablation using an electronically focused phased array: A theoretical analysis of patient safety. *Medical physics*, 41(7), 2014.

[48] Jie Sun and Kullervo Hynynen. Focusing of therapeutic ultrasound through a human skull: a numerical study. *The Journal of the Acoustical Society of America*, 104(3):1705–1715, 1998.

[49] Paul A Yushkevich, Joseph Piven, Heather Cody Hazlett, Rachel Gimpel Smith, Sean Ho, James C Gee, and Guido Gerig. User-guided 3d active contour segmentation of anatomical structures: significantly improved efficiency and reliability. *Neuroimage*, 31(3):1116–1128, 2006.

[50] Qianqian Fang and David A Boas. Tetrahedral mesh generation from volumetric binary and grayscale images. In *Biomedical Imaging: From Nano to Macro, 2009. ISBI'09. IEEE International Symposium on*, pages 1142–1145. Ieee, 2009.

[51] Aki Pulkkinen, Beat Werner, Ernst Martin, and Kullervo Hynynen. Numerical simulations of clinical focused ultrasound functional neurosurgery. *Physics in Medicine & Biology*, 59(7):1679, 2014.

[52] James R Fienup. Invariant error metrics for image reconstruction. *Applied optics*, 36(32):8352–8357, 1997.

[53] Harvey B Mitchell. *Image fusion: theories, techniques and applications. Chapter 14: Image Similarity Measures*. Springer Science & Business Media, 2010.

[54] Richard SC Cobbold. *Foundations of biomedical ultrasound*. Oxford University Press, 2006.

[55] Pascal Droin, Genevieve Berger, and Pascal Laugier. Velocity dispersion of acoustic waves in cancellous bone. *IEEE transactions on ultrasonics, ferroelectrics, and frequency control*, 45(3):581–592, 1998.

[56] Keith A Wear. The effects of frequency-dependent attenuation and dispersion on sound speed measurements: applications in human trabecular bone. *IEEE transactions on ultrasonics, ferroelectrics, and frequency control*, 47(1):265–273, 2000.

[57] Constantin-C Coussios, Christy K Holland, and George J Shaw. Transmission of a large unfocused 120-khz and 1-mhz ultrasound beam through the human skull. *The Journal of the Acoustical Society of America*, 112(5):2433–2433, 2002.

[58] Meaghan A O'Reilly, Yuexi Huang, and Kullervo Hynynen. The impact of standing wave effects on transcranial focused ultrasound disruption of the blood–brain barrier in a rat model. *Physics in Medicine & Biology*, 55(18):5251, 2010.

[59] Gianmarco F Pinton, Jean-Francois Aubry, and Mickael Tanter. Direct phase projection and transcranial focusing of ultrasound for brain therapy. *IEEE transactions on ultrasonics, ferroelectrics, and frequency control*, 59(6):1149–1159, 2012.

[60] James L Berry, James M Moran, William S Berg, and Arthur D Steffee. A morphometric study of human lumbar and selected thoracic vertebrae. *Spine*, 12(4):362–367, 1987.

[61] Jason White, Greg T Clement, and Kullervo Hynynen. Transcranial ultrasound focus reconstruction with phase and amplitude correction. *ieee transactions on ultrasonics, ferroelectrics, and frequency control*, 52(9):1518–1522, 2005.